Development of characterization tools for reliability testing of MicroElectroMechanical system actuators

Norman F. Smith[*], William P. Eaton, Danelle M. Tanner, and James J. Allen

Sandia National Laboratories, P.O. Box 5800, MS 1081, Albuquerque, NM 87185-1081

ABSTRACT

Characterization tools have been developed to study the performance characteristics and reliability of surface micromachined actuators. These tools include 1) the ability to electrically stimulate or stress the actuator, 2) the capability to visually inspect the devices in operation, 3) a method for capturing operational information, and 4) a method to extract performance characteristics from the operational information.

Additionally, a novel test structure has been developed to measure electrostatic forces developed by a comb drive actuator.

Keywords: MicroElectroMechanical Systems, MEMS Actuator Reliability, MEMS Characterization, Performance Tools, Image Analysis

1. INTRODUCTION

The microelectronics industry has long had a large suite of tools for performing characterization, parameter extraction, and reliability testing of integrated circuits. These tools are supplied by a large number of various manufacturers. As MEMS become more commercially feasible, a new set of measurement tools is needed.

MEMS are typically classified into two types, sensors and actuators. The characterization of MEMS sensors can be performed with the same types of tools that are used in the microelectronics industry. These sensors typically output an electrical signal that is easily measured, with the input stimulus coming from a controllable environmental condition. However, the MEMS actuator (e.g. – Sandia fabricated microengine in Figure 1) is much more difficult to characterize since it performs work based on its input stimulus. The work that is performed, ranging from rotating a gear transmission to popping up a mirror[1, 2], is not easily meas-
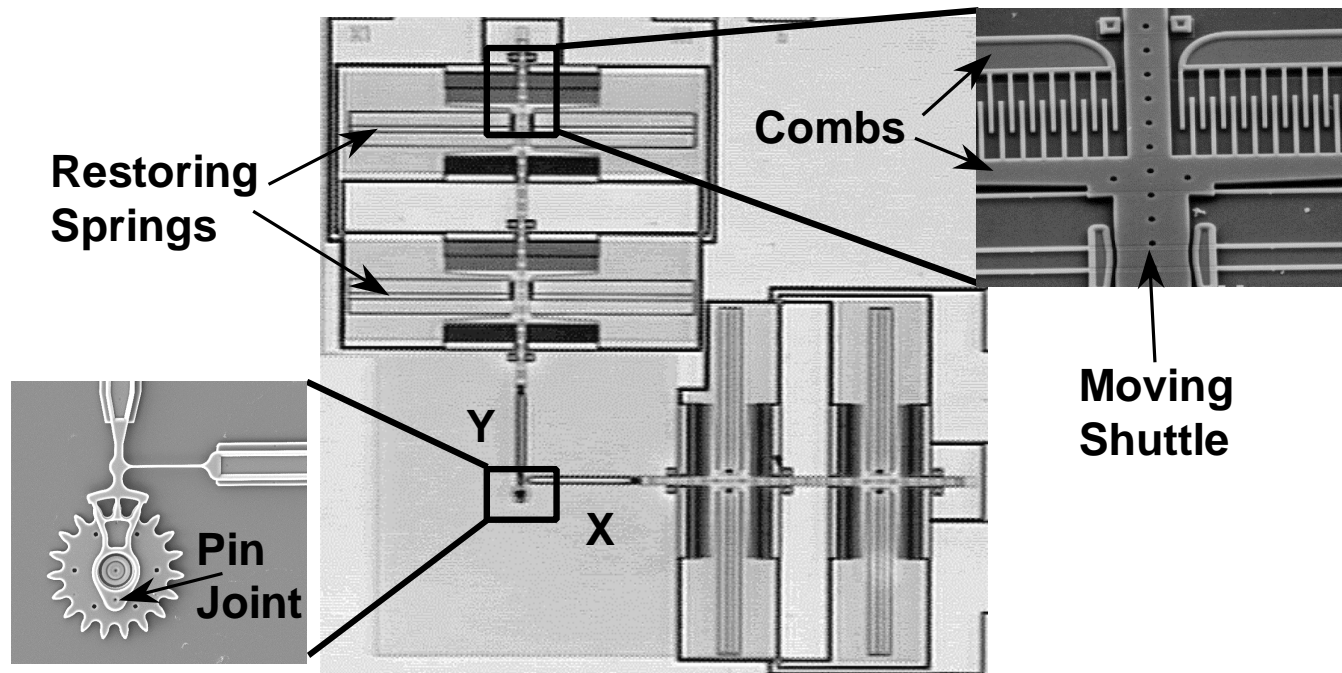
Figure 1. Sandia microengine with expanded views of the comb drive (top right) and the rotating gear (bottom left) shown in what we define at θ = 0.

*Correspondence: Email: smithnf@sandia.gov; WWW: http://www.mdl.sandia.gov/Micromachine

ured by electrical methods, where as results are readily measured using optical diagnostic techniques.

We will present the development of tools to characterize and test the reliability of the Sandia designed microengine.[3] The microengine consists of orthogonal linear comb drive actuators mechanically connected to a rotating gear as seen in Figure 1. By applying the proper drive voltages, the linear displacement of the comb drives is transformed into circular motion. The X and Y linkage arms are connected to the gear via a pin joint. The gear rotates about a hub, which is anchored to the substrate.

2. TOOL DEVELOPMENT

2.1. Super μDriver
The microengine can be driven with standard function generator waveforms by removing the positive or negative lobe of the waveform. However, this type of waveform results in excessive forces on the gear, hub and pin joint resulting in premature failure of the device. Therefore, a more customized or model-based drive signal is required to properly operate the microengine[4]. This requirement has led to the development of flexible waveform generation software and hardware that can generate model-based drive signals as well as standard function generator waveforms. This system is referred to as the Super μDriver. Figure 2 shows a representation of the parameters required to operate the microengine reliably.

The microengine comb drive is attached to the Y linkage arm in an asymmetric manner, which requires the up drive signal to be larger than the down drive signal. The comb drive is attached to the X linkage arm so that the left and right drive signals are equal (Figure 1). The basic drive signal configuration is shown in Figure 3. The Super
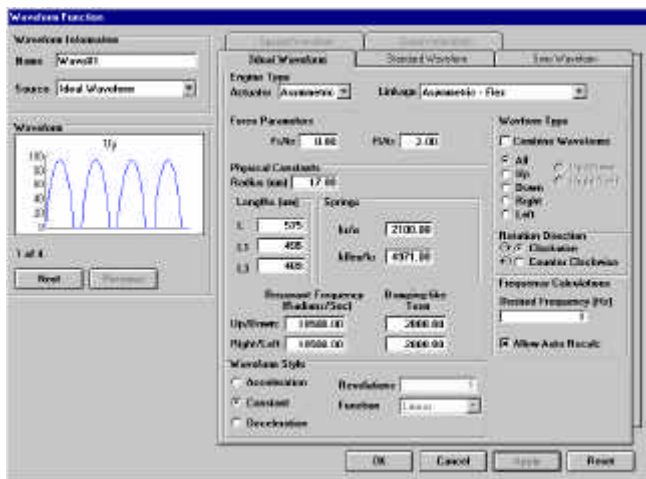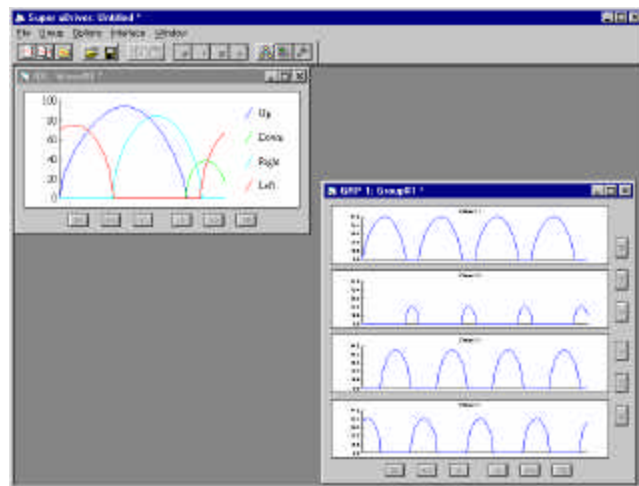
Figure 3. A typical set of drive signals for the microengine.

μDriver software enables these model-based drive signals to be linked together to provide the necessary signals to rotate the gear a preset number of revolutions and change directions as shown in Figure 4 and Figure 5.
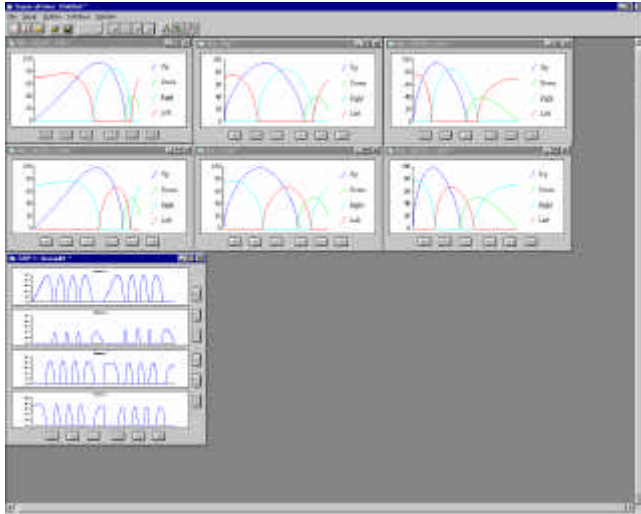
2.2. SHiMMeR
The Super μDriver reliably operates the microengine. However, a method to inspect the operation and performance of the engine on a statistically significant number of parts was required. The tool developed known as SHiMMeR (Sandia High Volume Measurement of Micromachine Reliability)[5] was employed to perform this task.

2.2.1. SHiMMeR design
The SHiMMeR system was designed and built to provide electrical drive signals to large numbers of packaged micro-actuators and to optically inspect them for functionality. SHiMMeR is subdivided into the electrical subsystem, which provides optimized electrical signals to the packaged parts, and the optical subsystem, in which a microscope and camera are stepped from part to part to inspect functionality. The optical system for SHiMMeR consists of two major components; an X-Y gantry table, and a video microscope (Figure 6).

The X-Y gantry table used to build the SHiMMeR system is a Techno Isel Gantry System III table with a travel of 500 x 540 mm, a table size of 850 x 750 mm, and a 200 mm clearance under the Z axis. This table has a repeatability of 10 μm and can support a payload of 22.7 kg on the Y axis. The axes are driven by Parker Compumotor Indexers that provide a resolution of 1.25 μm, when used with the standard 5mm pitch ball screw on the table. The overall accuracy of the table is ±0.1 mm over 300 mm. A high accuracy table was not required for this application because MEMS devices have considerable variation when mounted inside packages and the test fixture also varies somewhat. These

Figure 2. Waveform function screen showing drive signal parameters required to properly operate the microengine.

Figure 4. An example of linking drive signals together to create useful motion. These signals are used to move a linear rack assembly back and forth (Figure 5).
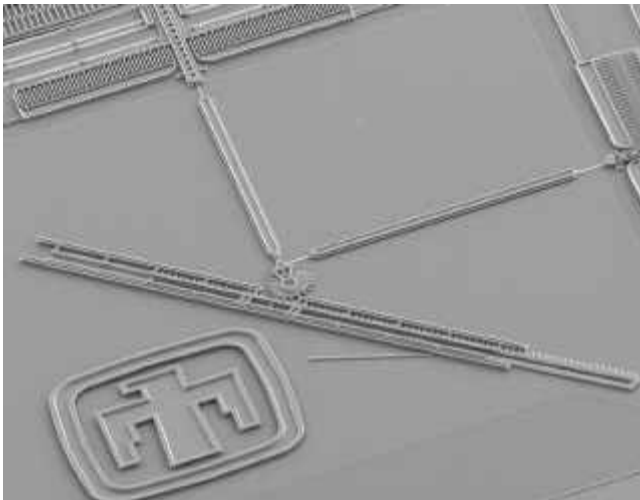
Figure 5. SEM of a microengine driving a linear rack assembly.

variations prevent exact determination of where the part is located within the travel of the gantry table, thus negating the requirement for accurate linear distance moves. Currently the operator of the SHiMMeR system is required to manually teach the system the location of each MEMS device being characterized prior to the start of a test.

The video microscope used in SHiMMeR is a 9x A-Zoom microscope from Ready Products Corporation. This microscope has many features that made it very useful in our system. It uses a single lens for its entire magnification range. In our configuration with a 20x long working distance objective, the magnification is continuously variable from 250x to 1800x with a field of view ranging from 1.1 mm to 150 μm on a 13 inch monitor. This allows the SHiMMeR

Figure 6. X-Y gantry table showing the socket arrangement and video microscope.

system to look at a wide variety of MEMS devices without the operator having to change primary objectives, thus eliminating the possibility that a turret full of lenses would collide with other parts of the system. The microscope is equipped with motorized focus controls and illumination is provided through a 150W fiber optic light source and/or a stroboscopic light source. All aspects of the microscope can be controlled from a personal computer via an RS-232 port. A high-resolution black and white CCD camera is used for acquisition of the image.

The stimulus or stressing system is made up of several components: waveform synthesis, waveform amplification, waveform distribution, and MEMS device fixtures. The waveforms are created using the prior version of the Super μDriver software described earlier. The new version of the waveform software is being incorporated into SHiMMeR. This will allow multiple stress conditions to be applied simultaneously to different devices under test. Waveforms for driving the MEMS devices are created using four 20 MHz arbitrary waveform generators from Pragmatic Instruments. All four channels are phase-locked together and use a common clock. The model-based waveforms are downloaded via IEEE-488.2 bus to the waveform generators.

The maximum output voltage from the waveform generators is limited to ±10V. Since this voltage is insufficient to actuate our electrostatic comb drives of the SNL microengine, the output waveforms must be amplified to a voltage sufficient to drive the device. Amplification is achieved with a custom 4-channel amplifier designed and built at SNL. The amplifier provides up to a 200V drive signal for the electrostatic combs and has a bandwidth sufficient to drive the microengines up to 600,000 rpm.

The device fixture consists of modular printed circuit boards with 8 24-pin DIP sockets. All sockets on the board are wired in parallel with each pin isolated from the parallel bus via 1 MΩ resistors. This provides the needed isolation from

one device short-circuiting and causing the remaining devices to stop functioning due to missing drive signals. The test bed consists of a 4 x 2 array of these printed circuit boards (Figure 6). This arrangement of multiple small printed circuit boards rather than one large board provides great flexibility in the arrangement, device wiring, and signal optimization of MEMS devices under test.

Waveform distribution is controlled through a manual switch matrix. The current matrix is arranged in a 6 x 24 arrangement. This arrangement accommodates the four drive signals required for the SNL microengine, a ground line, and a line that disconnects the socket pin from any signal. Additional switch matrices can be added by breaking up the 4 x 2 arrangement of the test fixture boards allowing for greater flexibility in testing.

The optical subsystem and device fixtures are enclosed within a custom Plexiglas enclosure. This enclosure is humidity controlled. The humidity control range is from 2 to 90+ % RH. This control is accomplished through two separate systems. A gas bubble system is used for humidity control between 2% to 45% RH. The humidity plane over the DUTs can be controlled to within ±0.2%. The second unit is a standard steam humidifier. This system is used above 45% RH and controls humidity levels to within ±5%. A chilled mirror hygrometer is used to measure the actual humidity levels encountered during testing.

The entire system (optics, DUTs, and the humidity enclosure) is mounted on a vibration isolation table. This provides us with the ability to remove any ambient laboratory vibration from entering into our experimental data. It also allows us to achieve high magnification of our devices without experiencing blurring due to external vibrations. The humidity and vibration isolation systems are illustrated in Figure 7.

2.2.2. Reliability testing software
The software developed to run the SHiMMeR system was written using Visual Basic. This software allows the operator to optimize and vary all engine drive signal parameters. The amplitude and shape of the drive signals can be viewed on the monitor, prior to application to the devices under test. Test fixture arrangements that can be made to fit within the travel of the X-Y gantry table as well as layouts of the MEMS device can be accommodated through description files created by the software.

The operator test screen allows stress and duration parameters to be defined and varied throughout the test. A running commentary can be kept on each device under test until it fails, at which time the software will skip the observation portion of the test unless set up to do otherwise. Device failures are currently broken down into three major categories where each category can have one level of sub-categories.


Figure 7. Vibration isolation and humidity enclosure for SHiMMeR. Doors have been removed for clarity.

The operator can use the predefined sub-categories or add additional ones as the test progresses. A color-coded map of the test bed displays the current status of each package under test as well as the status of each device in each package (Figure 8).

2.2.3. Data extraction
Currently, most of the data is taken manually from the SHiMMeR system, while an automated system is being completed. The operator defines the test by establishing a series of stress and inspection cycles. The stress cycles operate the microengine at high speed, while the inspection cycle slows the microengine down to 1 Hz, a speed that is easily viewable by the operator. The operator can then visually inspect each microengine and note its functionality. The operator has the option of using a stroboscopic light source to view the microengine during its high-speed stress cycle. This manual method to perform reliability experi-
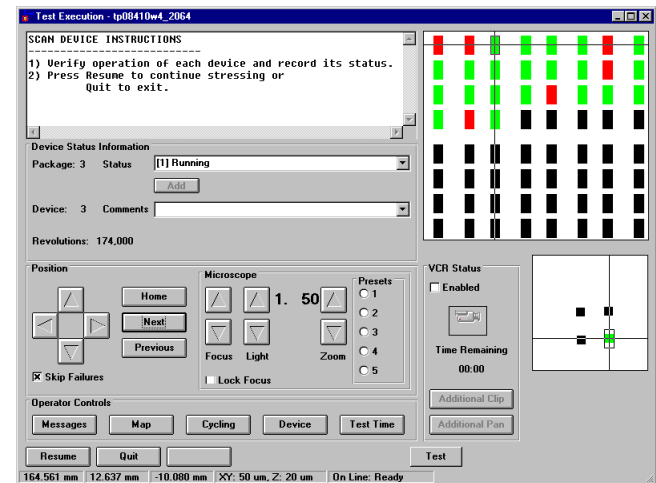

Figure 8. Operator's test control panel for SHiMMeR. This panel displays the currently status of the devices under test.

ments has been successfully employed. [5,6] However this is a very labor-intensive process.

In order to address the problems associated with operator variability (parallax, narrative descriptions, fatigue, etc.), steps toward full automation have been made. We are incorporating an image capture and analysis system into our suite of MEMS tools. Others have reported similar systems. [7,8]

2.3. Image capture and analysis

A high intensity stroboscopic light (Olympus ALS-12000S) source is used for illumination of the DUT at operational speeds. This light source is directly coupled into the same fiber optic bundle that is used for normal illumination. The flash rate can be externally controlled with an approximate flash duration of 3-5μs. A National Instruments TCIO-10 timer/counter card and a National Instruments Monochrome Video capture card handle the timing of the strobe and the image snapshots. The timer/counter tracks the actual drive signal operating the device through a timing signal generated by the arbitrary waveform generators. The strobe light is unable to fire at the drive rates routinely encountered, so an additional counter is configured as a divide-by-N. This generates a new flash rate that the strobe can constantly lock onto. One other counter is configured to generate a finely controlled delayed pulse for the strobe and image capture card. This delay allows images to be acquired at any desired angle during the waveform period. A schematic of the control system is shown in Figure 9.
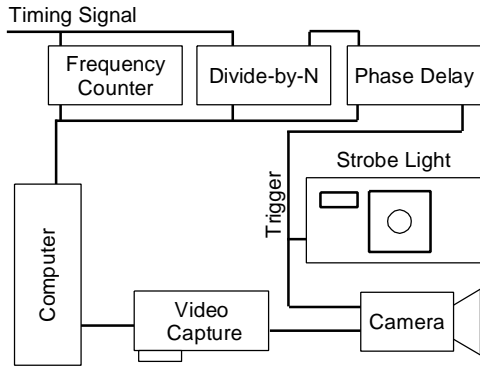
**Figure 9.** Block diagram of image capture system.

Additional software has been developed to fully control this image capture system. The system has been designed to handle the large number of images and devices that can be characterized on the SHiMMeR system.

3. TEST STRUCTURE DEVELOPMENT

In order to characterize an electrostatic actuator, the spring constant and force output of the actuator must be determined. The measurement of force output requires the actuator to move a known structure (typically a cantilever beam) a measurable distance. Bending equations are then used to calculate the force. We will describe a novel test structure called the 'force detector' and the complete techniques used to determine force and spring constant.

The force detector consists of a ring of polysilicon anchored to the substrate at one location and attached to the actuator 180 degrees from the anchor as shown in Figure 10. The ring radius is 250 μm and the width of the ring was 4 μm. The ring thickness was defined in our process to be 2.5 μm. Pulling from the actuator end will elongate the ring and deflections are measured in three locations (X, Y1, and Y2). A closer view of the calibration tick marks (each mark is 1 μm wide and they are separated by 1 μm) are shown in Figure 11. The upper SEM image shows the ring in relation to the tick marks and the higher level polysilicon strap used to prevent curl in the structure. The lower SEM image is a closer view of the actuator attachment to the ring. Note the tick marks used for deflection measurement.
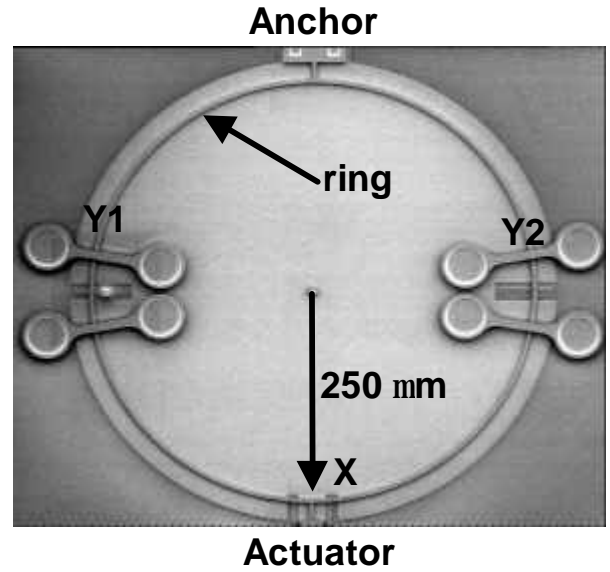
Figure 10. This SEM image of the force detector shows the ring and the location of the anchor and actuator.

Standard formulas for circular rings were used to calculate the force necessary to cause deflection. [9] For deflection toward the actuator (D_x), we have

$$D_X = 0.137 \frac{Fr^3}{EI} \tag{1}$$

where r is the radius of the ring, E is Young's modulus for polysilicon (0.155 N/μm^2), and I is the bending moment. A similar equation exists for deflections in the y direction (D_Y),
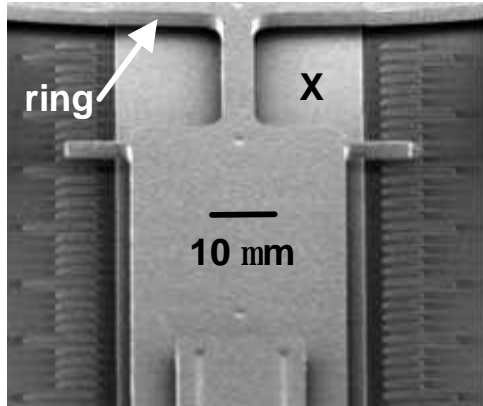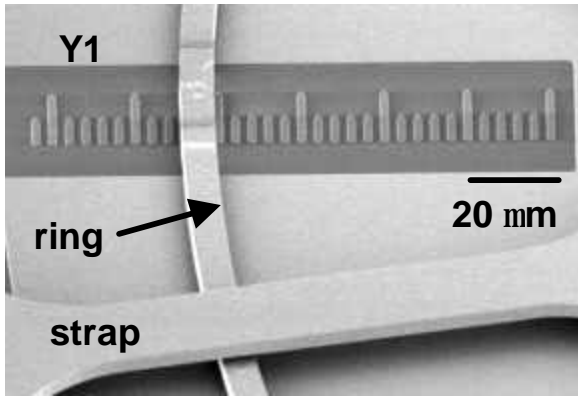
Figure 11. The upper SEM image shows the Y1 deflection measurement. Note the ring and the higher-level polysilicon strap. The X deflection measurement arm that attaches to the actuator is shown in the lower
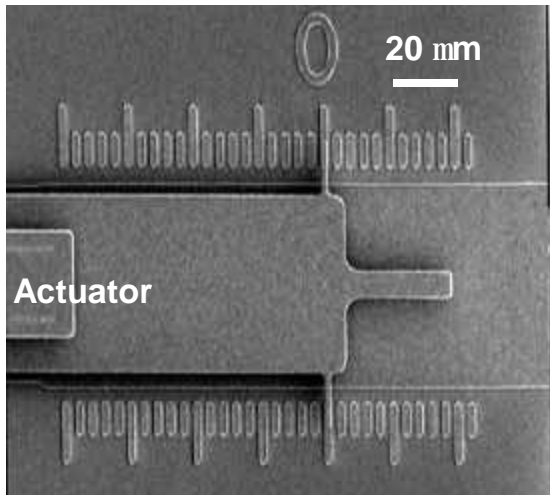
Figure 12. The gage to determine spring constant is shown. The actuator (not shown) can pull (move to the left) or push the gage.

$$D_Y = D_{Y1} + D_{Y2} = -0.149 \frac{Fr^3}{EI} \qquad (2)$$

where the negative sign indicates movement toward the center of the ring. The bending moment, I, is $I = bw^3/12$ where w is the width of the ring (4 μm) in the plane and b is the polysilicon layer thickness (2.5 μm).

Equations 1 and 2 can be solved for force, F, so that when we apply a voltage and measure a deflection, calculating the force is straightforward. In electrostatics, $F = -aV^2$, where the minus sign indicates an attractive force. The constant, a, is simply the slope of F versus V^2.

The determination of spring constant, k, requires a simpler structure consisting of an actuator and a gage. Figure 12 shows the gage used for this measurement; the actuator was located to the left of the figure and is not shown. The tick marks were fabricated in the poly0 level and the movable gage was fabricated in an upper poly2 level. Voltage was applied to the actuator which caused deflections, x, in the gage. We then plot V^2 versus x and use the equations, $F = kx = aV^2$, to calculate the slope, k/a. The earlier value of a combined with this result will yield a value for k.

4. RESULTS AND DISCUSSION

The MEMS device used in our development of these tools and the majority of our experiments is an electrostatically driven microactuator (microengine) developed at Sandia National Laboratories.

4.1 Super μDriver
The Super μDriver has proven to be a valuable tool. It was designed with enough flexibility and capability to provide the necessary drive signals required to properly operate complex devices that are powered by the microengine. Currently up to eight microengines can be controlled with each one operating with different drive signal parameters. A microlock[10] shown in Figure 13 presents an example of a complex device that can be operated with this software.

4.2 SHiMMeR
The development of Super μDriver and SHiMMeR has allowed device characterization on statistically significant numbers of MEMS devices. We have the ability to control multiple aspects of device operation as well as environmental conditions. The ability to perform these lifetime testd have allowed us to gain an understanding of how these devices fail. Results of these lifetime experiments have been published elsewhere.[5, 6, 11, 12, 13]
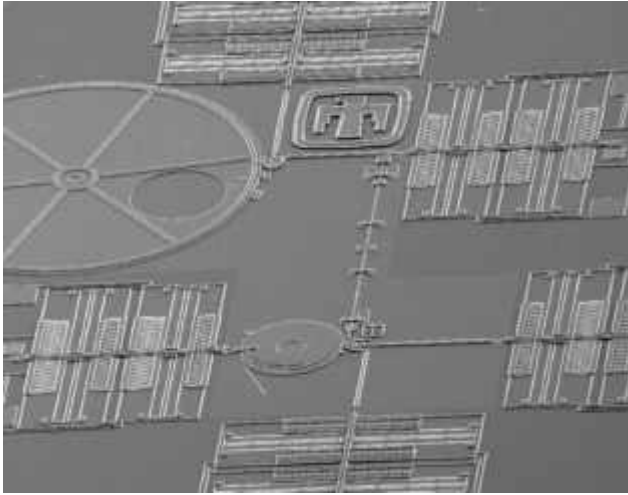
**Figure 13.** SEM of a surface micromachined lock and optical shutter assembly.

4.1 Image Analysis

The ability to capture and analyze images captured at operational speeds has allowed a more qualitative assessment of microengine performance. It has also provided the ability to compare various design modifications against one another. This analysis has allowed design enhancements that increased the reliability of the microengine. In order to study unconstrained operation of the microengine, removal of the gear is necessary. This allows the drive signals and inherent device behavior to be determined. Figure 14 shows an example of a microengine design that exhibits linear clamping. The linear clamping is due to the fringe field forces becoming non-linear at the end of their full engagement. This design can be contrasted with the design shown in Figure 15. In this design the linear clamping problem has been eliminated. This device still exhibits some non-ideal effects due to frictional forces changing during the rotation of the device. The flat sections of the curves are where the shuttle is pressing against the guides with enough force to prevent them from sliding efficiently.

4.2 Test Structures

The voltage was adjusted on the force detector actuator to yield displacement steps in the X gage of 2 μm. Data from five force detectors is shown in Figure 16. Each set of data was analyzed using linear regression and the slope was determined. The average a using this technique was $1.34 \pm .06 \times 10^{-4}$ μN/V^2.

Data from the gage shown in Figure 12 was acquired in the same manner. The voltage in the actuator was adjusted to yield displacement steps of 2 μm. Data from five gages is shown in Figure 17 where each slope was determined. The average k/a was $60.2 \pm .3.9$ V^2/μm. For operation of a mi-
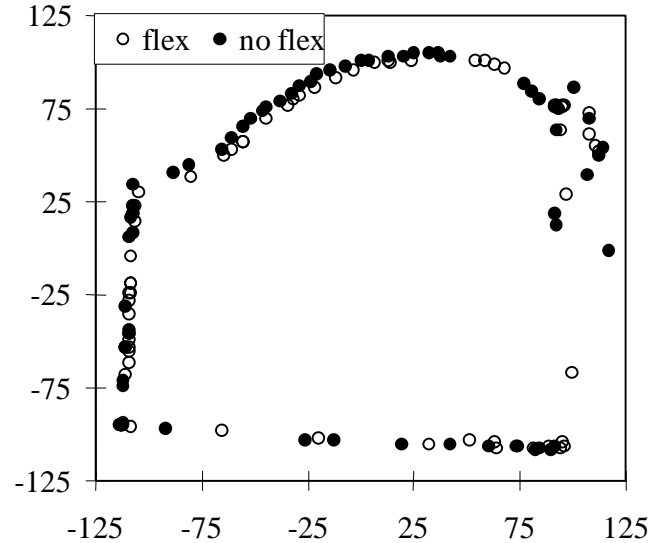
**Figure 14.** Position map of a gearless microengine with linear clamping and radius set to 17 μm. Horizontal and vertical axes are in pixels.
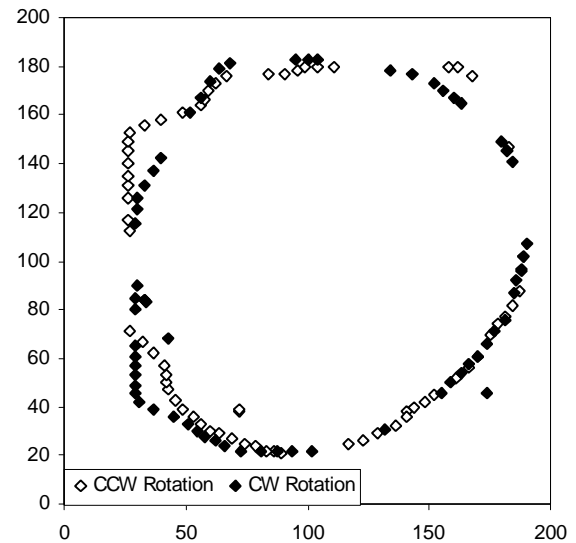

Figure 15. Position map of a gearless microengine without linear clamping and radius set to 17μm. Horizontal and vertical axes are in pixels. The flat sections in the rotation are due to increases in frictional forces of the shuttle against its guides.

croengine, the actuator must move at least 29 μm and that displacement is noted on the graph.
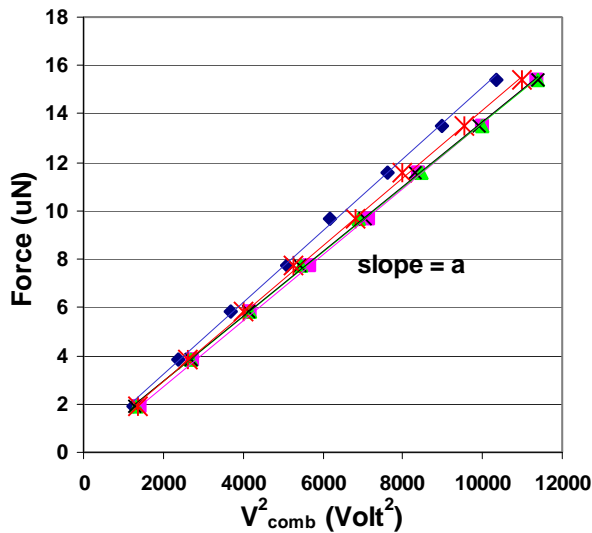
Figure 16. Data from the force detector. The electrostatic constant, *a,* was determined from the slope.
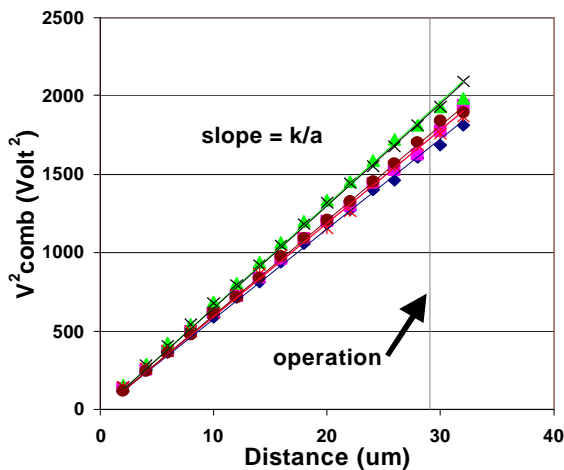
Figure 17. Data from the actuator and gage are shown. The actuator must move to the operation line in order for a microengine to run.

Both data sets reveal the variation in the fabricated devices. The value of spring constant was calculated as .083 ± .0065 N/m that has a combined error of roughly 10%.

5. CONCLUSIONS

We have successfully developed both hardware and software tools for reliability testing of microactuators. SHiM-MeR is being used routinely and has proven to be an extremely useful tool. The Super μDriver software was shown to be flexible and necessary to run complex actuator designs.

The image capture and analysis methods are viable methods for determining engine degradation. More work is currently underway to integrate this system into the SHiMMeR system for reliability testing. Additional work is also required to try to minimize or eliminate the inherent averaging measurements that this method produces.

The force detector has enabled calibration of our comb actuator. The same structure and technique could be used on any actuator.

ACKNOWLEDGMENTS

REFERENCES

1. J. J. Sniegowski, "Multi-level polysilicon surface micromachining technology: applications and issues, "*Proceedings of the ASME Aerospace Division*, **Vol. 52**, 1996, pp. 751-759.
2. http://www.mdl.sandia.gov/Micromachine/
3. S. L. Miller, J. J. Sniegowski, "Surface micromachined microengine", Sensors and Actuators A, **Vol. 48**, 1995, pp. 203-214.
4. S. L. Miller, J. J. Sniegowski, G. LaVigne, and P. J. McWhorter, "Performance tradeoffs for a surface micromachined microengine", *Proceedings of SPIE Micromachined Devices and Components II*, **Vol. 2882**, Austin, October 14-15, 1996, pp. 182-191.
5. D. M. Tanner, N. F. Smith, D. J. Bowman W. P. Eaton, K. A. Peterson, "First Reliability Test of a Surface Micromachined Microengine Using SHiMMeR", *Proceedings SPIE Symposium on Micromachining and Microfabrication*, **Vol. 3224**, Austin, 1997, pp. 14-23.
6. D. M. Tanner, W. M. Miller, W. P. Eaton, L. W. Irwin, K. A. Peterson, M. T. Dugger, D. C. Senft, N. F. Smith, P. Tangyunyong, and S. L. Miller, "The Effect of Frequency on the Lifetime of a Surface Micromachined Microengine Driving a Load", *Proceedings International Reliability Physics Symposium*, Reno, 1998, pp. 26-35.
7. D. M. Freeman and C. Q. Davis, "Using Video Microscopy to Characterize Micromechanics of Biological and Man-made Micromachines", *Technical Digest of the 1996 Solid-State Sensor and Actuator Workshop*, Hilton Head Isl., June 3-6, 1996, pp. 161-167.

8. G. F. LaVigne and S. L. Miller, "A Performance Analysis System for MEMS using Automated Imaging Methods", *IEEE International Test Conference*, Washington DC, Oct. 18-23, 1998, pp. 442-447

9. R. J. Roark, "*Formulas for Stress and Strain*," Fourth Version, McGraw-Hill Book company, p. 172, 1965.

10. M. S. Rodgers, J. J. Sniegowski, S. L. Miller, C. C. Barron, and P. J. McWhorter, "Advanced micromechanisms in a multi-level polysilicon technology," Proc. of SPIE, 3224, Austin, TX, (1997), pp. 120-130.

11. D. M. Tanner, W. M. Miller, W. P. Eaton, L. W. Irwin, K. A. Peterson, M. T. Dugger, D. C. Senft, N. F. Smith, P. Tangyunyong, and S. L. Miller, "The Effect of Frequency on the Lifetime of a Surface Micromachined Microengine Driving a Load," *Proceedings. International Reliability Physics Symposium*, 1998, pp. 26-35.

12. D. M. Tanner, L. W. Irwin, W. P. Eaton, N. F. Smith, K. A. Peterson, and W. M. Miller, "Linkage Design Effect on the Reliability of Surface Micromachined Microengines Driving an Inertial Load," *Proceedings SPIE Symposium on Micromachining and Microfabrication*, Santa Clara, CA, **Vol. 3512**, pp.215-226.

13. D. M. Tanner, J. A. Walraven, L. W. Irwin, M. T. Dugger, N. F. Smith, W. M. Miller, and S. L. Miller, *"The Effect of Humidity on the Reliability of a Surface Micromachined Microengine," Proceedings International Reliability Physics Symposium*, 1999, pp. 189-197.